

# Hele–Shaw flow and pattern formation in a time-dependent gap

Michael J Shelley, Fei-Ran Tian<sup>†</sup> and Krzysztof Wlodarski

Courant Institute, New York University, New York, NY 10012, USA

Received 22 October 1996, in final form 19 June 1997

Recommended by S Kida

**Abstract.** We consider flow in a Hele–Shaw cell for which the upper plate is being lifted uniformly at a specified rate. This lifting puts the fluid under a lateral straining flow, sucking in the interface and causing it to buckle. The resulting short-lived patterns can resemble a network of connections with triple junctions. The basic instability—a variant of the Saffman–Taylor instability—is found in a version of the two-dimensional Darcy’s law, where the divergence condition is modified to account for the lifting of the plate. For analytic data, we establish the existence, uniqueness and regularity of solutions when the surface tension is zero. We also construct some exact analytic solutions, both with and without surface tension. These solutions illustrate some of the possible behaviours of the system, such as cusp formation and bubble fission. Further, we present the results of numerical simulations of the bubble motion, examining in particular the distinctive pattern formation resulting from the Saffman–Taylor instability, and the effect of surface tension on a bubble evolution that in the absence of surface tension would fission into two bubbles.

PACS numbers: 4720D, 4720M, 4755D, 8385P

AMS classification scheme numbers: 76E30, 76D45

## 1. Introduction

Informal observations of interfacial motion in a Hele–Shaw cell show that very intricate and atypical patterns can form in a liquid/gas interface as the upper plate is lifted [35]. This lifting puts the fluid under a lateral straining flow, sucking in the interface and causing it to buckle. This basic mechanism, though coupled to a much different material rheology, is likely to be responsible for producing the permanent patterns left behind after pulling up some adhesive tapes. The resulting short-lived patterns can resemble a network of connections with triple junctions. Similar patterns are observed in Hele–Shaw experiments where one of the glass plates was lifted by one edge. This makes the gap time and space dependent (see [6, 36, 30, 21]).

Here we assume that the upper plate is lifted uniformly—that is, the gap width is a function of time, but not of space. This gives a relatively simpler situation wherein the basic instability can be studied, some mathematical analysis can be made, and detailed numerical simulations performed. Recently McCloud and Maher [22] have recently reviewed similar and many other experimental variants of Hele–Shaw flow.

In a typical experiment (or simulation) of pattern formation in a radial Hele–Shaw cell, a less viscous fluid (say a gas) is pumped into a more viscous fluid. The usual scenario for the

<sup>†</sup> Current address: Department of Mathematics, The Ohio State University, Columbus, OH 43210, USA.

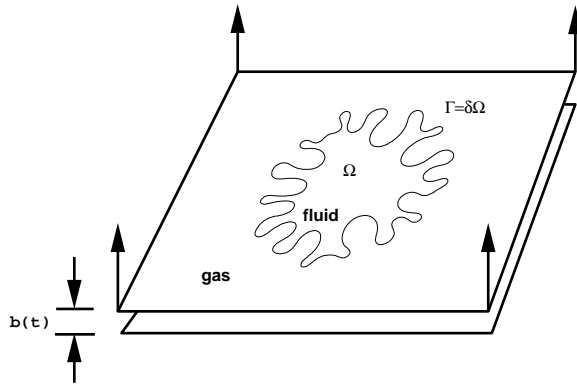


**Figure 1.** A schematic diagram of the bubble in the Hele–Shaw cell.

nonlinear development of the Saffman–Taylor instability is the appearance of growing petals. A petal’s radius of curvature increases in time until it is comparable with the wavelength of an unstable mode. The petal tip then splits, engendering new petals (and fingers), which themselves grow and split, with the process eventually giving rise to a dense branching morphology [5]. A much different pattern formation scenario is observed for a plate lifting over a patch of fluid surrounded by gas. The liquid/gas interface rushes inwards, forming structures similar to Saffman–Taylor fingers. When the length of the fingers are comparable with the width of the bubble, they interact strongly with each other, and compete within an ever decreasing bubble area (see figure 1). This competition can create a network-like structure of branches tipped with attached droplets. While the driving physics is apparently much different, these patterns are visually similar to those seen in ferro-fluid labyrinths [20].

The basic instability—a variant of the Saffman–Taylor instability—is found in a version of the two-dimensional Darcy’s law, where the divergence condition is modified to account for the lifting of the plate. The use of Darcy’s law implies that we are assuming that the plate is not being lifted fast enough to provoke any inertial effects, nor lifted high enough to alter the system being of large aspect ratio.

As our model, we consider a modified Hele–Shaw flow within a bubble in the  $xy$ -plane (see figure 1), its area is denoted by  $\Omega(t)$  with boundary  $\partial\Omega(t)$ . Our model system is given by:

$$\mathbf{u}(x, y, t) = -\frac{b(t)^2}{12\mu} \nabla p(x, y, t) \quad \text{in } \Omega(t) \quad (1.1)$$

$$\nabla \cdot \mathbf{u} = -\frac{\dot{b}(t)}{b(t)} \quad \text{in } \Omega(t) \quad (1.2)$$

$$p = \tau\kappa \quad \text{on } \partial\Omega(t) \quad (1.3)$$

$$V_n = -\frac{b(t)^2}{12\mu} \frac{\partial p}{\partial \mathbf{n}} \quad \text{on } \partial\Omega(t). \quad (1.4)$$

Equation (1.1) is Darcy’s Law, where  $\mathbf{u} = (u, v)$  is the two-dimensional gap-averaged velocity,  $p$  is the pressure,  $b(t)$  is a (prescribed) time-dependent gap width, and  $\mu$  is the fluid viscosity. Equation (1.2) expresses conservation of volume for the fluid mass, and is a modification of the usual two-dimensional divergence-free condition. We take the traditional Laplace–Young boundary condition for the pressure (1.3), where  $\tau$  is a surface tension coefficient, and  $\kappa$  is the curvature of  $\partial\Omega(t)$ .  $V_n$  is the normal component of the

boundary velocity and  $\mathbf{n}$  is the outward unit normal vector to  $\partial\Omega(t)$ . Hence, condition (1.4) requires that the boundary  $\partial\Omega$  moves with the fluid. The Darcy’s law is derived from Navier–Stokes equations in the usual way for Hele–Shaw flow; we remark only on divergence condition (1.2). Let  $z$  be the coordinate across the gap, with velocity  $w$  in that direction. Holding the bottom plate fixed at  $z = 0$ , we average the full three-dimensional divergence-free condition,

$$0 = \frac{1}{b(t)} \int_0^{b(t)} (u_x + v_y + w_z) dz = \bar{u}_x + \bar{v}_y + (w|_{z=b(t)} - w|_{z=0})/b(t) \\ = \bar{u}_x + \bar{v}_y + \dot{b}(t)/b(t)$$

dropping the bars and moving the velocity terms to the right-hand side gives result (1.2). It is straightforward to verify that  $\text{Area}(\Omega(t)) \cdot b(t) = \text{Area}(\Omega(0)) \cdot b(0)$  where  $\Omega$  is any material area—this is conservation of fluid volume.

We nondimensionalize equations (1.1)–(1.4) as follows.  $x$  and  $y$  are scaled on the initial bubble diameter  $L_0$ . Time is scaled by the characteristic time  $T = b_c/|\dot{b}_c|$ , where  $b_c$  and  $\dot{b}_c$  are characteristic values of  $b$  and  $\dot{b}$ , respectively; here we will just take their initial values. Likewise,  $b(t)$  is scaled on its initial value. Finally, the pressure  $p$  is scaled on  $12\mu L_0^2/(Tb_c^2)$ . Retaining the same variable names, the nondimensional equations are

$$\mathbf{u} = -b(t)^2 \nabla p \quad \text{and} \quad \nabla \cdot \mathbf{u} = -\frac{\dot{b}(t)}{b(t)} \quad \text{in } \Omega(t) \quad (1.5)$$

$$p = \tilde{\tau} \kappa \quad \text{on } \partial\Omega(t) \quad (1.6)$$

$$V_n = -b(t)^2 \frac{\partial p}{\partial \mathbf{n}} \quad \text{on } \partial\Omega(t) \quad (1.7)$$

where  $\tilde{\tau} = \tau b_c^3/12\mu|\dot{b}_c|L_0^3$  is a nondimensional surface tension.

As for the classical Darcy’s law, the velocity  $\mathbf{u}$  is irrotational. However, the pressure is no longer harmonic and satisfies a Poisson equation:

$$\Delta p = \frac{\dot{b}}{b^3} \quad \text{in } \Omega \quad \text{with } p = \tilde{\tau} \kappa \quad \text{on } \partial\Omega \quad (1.8)$$

where its right-hand side depends only on time. The solution to this elliptic boundary value problem differs from being harmonic by only the simple particular solution,

$$\bar{p} = \frac{1}{4} \frac{\dot{b}}{b^3} (x^2 + y^2) \quad (1.9)$$

to equation (1.8). Its contribution can be interpreted as a straining velocity field that decreases the area of Lagrangian area elements.

A related problem is that of a bubble, in a fixed gap Hele–Shaw cell, where a mass sink, located at a point in the bubble, sucks fluid out. This problem has been studied, both numerically and analytically, most recently by Tian [31, 32] and by Nie and Tian [23]. This work shows that the interface will generically collide with the mass sink at some finite time, leading to a singularity. For the lifting plate, there is no such possibility, as the ‘mass sink’ is now uniformly distributed throughout the bubble area.

To explore the stability of our model system, consider the flow perturbed about the exact solution of an expanding or contracting circular bubble of radius  $R(t)$ . This is done conveniently in a complex variable form, where  $z(\alpha, t) = x(\alpha, t) + iy(\alpha, t)$  gives the location of  $\partial\Omega$  and is a periodic function of  $\alpha$ , a Lagrangian parametrization of  $\partial\Omega$  with  $0 \leq \alpha \leq 2\pi$ . Then, for  $\epsilon \ll 1$ , let

$$z(\alpha, t) = R(t)e^{i\alpha}(1 + \epsilon v) \quad \text{where } R(t) = R(0)\sqrt{b(0)/b(t)} \quad (1.10)$$

and  $v = \xi + i\eta$ . Expanding the equations and retaining  $O(\epsilon)$  terms yields the linear system:

$$\xi_t = -\frac{1}{2R^2}\mathcal{H}[\bar{\gamma}] \quad (1.11)$$

$$\eta_t = -\frac{1}{2R^2}\bar{\gamma} \quad (1.12)$$

$$\bar{\gamma} = -2\left[\frac{b^2}{R}\bar{\tau}(\xi_\alpha + \xi_{\alpha\alpha}) + \frac{\dot{b}}{2b}R^2\xi_\alpha\right] \quad (1.13)$$

where  $\mathcal{H}$  is the Hilbert transform (see [9]). This system is diagonalized by a Fourier transform in  $\alpha$ . At linear order,  $\xi$  is the radial perturbation from the circle. The instantaneous linear growth rate at wavenumber  $k$  is then

$$\sigma(k, t) = \frac{k\dot{b}}{2b} + \frac{b^2}{R^3}\bar{\tau}(k - k^3) \quad k \geq 0. \quad (1.14)$$

Thus, the circular bubble is linearly stable at all scales if  $\dot{b} < 0$ , i.e. the bubble is expanding. If the bubble is contracting, it is linearly unstable for  $k < \sqrt{1 + (\dot{b}R^3)/(2\bar{\tau}b^3)}$ , with the maximum growth rate at  $k_{\max} = \sqrt{1 + \dot{b}R^3/2\bar{\tau}b^3}/\sqrt{3}$ . A similar expression was also obtained by Zhao *et al* [36] for the ‘gap gradient’ case.

For  $\bar{\tau} = 0$ , we have the ill-posedness associated with an unregularized Saffman–Taylor instability. If  $\bar{\tau} > 0$ , then the instability is regularized at small length-scales, but with the additional, interesting aspect that the instability cannot be sustained as the plate is lifted and the bubble shrinks. This is quite unlike the more usual pattern formation problem of an expanding gas bubble in a Hele–Shaw cell. The important quantity is  $\dot{b}R^3/b^3$ , whose time-dependent part is  $\dot{b}/b^{9/2}$  (using equation (1.10)). If we require that  $\dot{b}/b^{9/2} \geq K^2 > 0$ , so that there will always be a band of unstable modes, it follows that  $b(t)$  becomes infinite at some finite time—an event clearly outside of the validity of our model. And so, for any monotonically increasing, smooth  $b(t)$ , the range of unstable modes will eventually collapse. For simplicity, we have made the choice for the gap width  $b(t) = e^t$ . As implied above, examination of equation (1.14) shows that  $k_{\max}$  decreases as  $t$  increases, and that  $\sigma$  is eventually negative for all  $k \geq 2$  ( $k = 0$  and  $1$  are only areal and translational perturbations, resp.). Even though this is only the result of a linear analysis, it is consistent with our simulations, given in section 3. They suggest that following a period of intense instability, the eventual behaviour of the bubble is to relax and circularize.

We make two further comments about the properties and structure of equations (1.5)–(1.7).

(i) When  $\bar{\tau} = 0$ , any explicit dependence of the dynamics upon  $b(t)$  can be absorbed into a redefinition of time and pressure. To see this most simply, assume that  $\dot{b} \neq 0$ , and let  $p = \frac{\dot{b}(t)}{b(t)^3}q$ . Then defining the new time  $s = \ln \frac{b(t)}{b(0)}$  gives the system as

$$\begin{aligned} \mathbf{u} &= -\nabla q & \text{and} & & \nabla \cdot \mathbf{u} &= -1 & \text{in } \Omega(t) \\ q &= 0 & \text{on } \partial\Omega(t) \\ V_n &= -\frac{\partial q}{\partial \mathbf{n}} & \text{on } \partial\Omega(t) \end{aligned}$$

which has no explicit dependence upon  $b$ . The time rescaling only appears when expressing  $V_n$  as the time derivative of interfacial position. As a consequence, two flows with the same initial bubble shape, but two different gap functions (both either increasing or decreasing) will evolve through the same set of shapes.

(ii) System (1.5) has a structure somewhat complementary to that of the ‘contour dynamics’ problem of two-dimensional Euler flow (see [37] for an early explication).

Contour dynamics concerns the evolution of a patch of constant vorticity fluid surrounded by irrotational fluid. There, the velocity field satisfies

$$\mathbf{u} = (-\psi_y, \psi_x) \quad \text{with } \Delta\psi = \chi(\Omega)$$

where  $\psi$  is the stream function, and  $\chi$  is the characteristic function for the domain  $\Omega$  (we have assumed unit vorticity). The Poisson equation is solved in the plane with continuity of  $\mathbf{u}$  across  $\partial\Omega$ , and appropriate far-field boundary conditions on  $\psi$ . Again using the same redefinition of pressure as above, system (1.5) can be rewritten in the form

$$\mathbf{u} = -(q_x, q_y) \quad \text{with } \Delta q = 1 \quad \text{in } \Omega.$$

In other words, for contour dynamics the velocity has zero divergence, and constant curl, at least in  $\Omega$ . For our problem, the velocity has zero curl, but constant divergence. Of course, the large differences lie in the domain of solution, and the boundary conditions; the contour dynamics problem is posed in the plane, while ours is interior to the bubble (the exterior gas pressure enters only as a removable constant) with the Laplace–Young boundary condition. While it has been proved for contour dynamics that the time-dependent boundary  $\partial\Omega(t)$  remains always smooth [10, 8], in the next section we show that it is easy to find exact solutions (when  $\tilde{\tau} = 0$ ) to our Hele–Shaw problem where  $\partial\Omega(t)$  becomes singular in a finite time.

In section 2, we use a Cauchy integral approach [32] to study the initial value problem for Hele–Shaw flows. For analytic data, we establish the existence, uniqueness and regularity of solutions when the surface tension is zero. We also construct some exact analytic solutions, both with and without surface tension. These solutions illustrate some of the possible behaviours of the system, such as cusp formation and bubble fission. In section 3, we present the results of numerical simulations of the bubble motion. In particular, we examine the pattern formation that results from the Saffman–Taylor instability, and also consider the effect of surface tension on a bubble evolution that in the absence of surface tension would fission into two bubbles.

## 2. Analytical results

### 2.1. Cauchy integral approach

Our analytic approach is similar to the one used to study a related problem, in a fixed gap Hele–Shaw cell, where a mass sink or source is located at a certain point in the bubble [24, 25, 32, 34]. Entov *et al* [15] made some preliminary analytical observations on the special case of ‘squeeze flow’, where  $\dot{b} < 0$ , and note a relation to a rotating Hele–Shaw flow.

We call a family of simply connected domain  $\{\Omega(t)\}$  smooth (analytic) if  $\partial\Omega(t)$  is a smooth (analytic) curve for each time  $t$ , and the velocity of  $\partial\Omega(t)$  continuously depends on time  $t$  and the arc length of the interface.

We first use (infinitely many) global quantities to capture the motion of the interface.

Following Richardson [24, 25, 32, 34], we consider the complex moments of the domain  $\Omega(t)$ :

$$\iint_{\Omega(t)} z^m \, dx \, dy$$

where  $z = x + iy$  for  $m = 0, 1, 2, \dots$

Calculating the time derivative of the moments, we obtain

$$\begin{aligned} \frac{d}{dt} \left[ \iint_{\Omega(t)} z^m dx dy \right] &= \int_{\partial\Omega(t)} z^m V_n ds \\ &= -b^2(t) \int_{\partial\Omega(t)} z^m \frac{\partial p}{\partial \mathbf{n}} ds \\ &= -b^2(t) \left[ \iint_{\Omega(t)} z^m \Delta p dx dy + \int_{\partial\Omega(t)} p \frac{\partial z^m}{\partial \mathbf{n}} ds \right] \\ &= -\frac{\dot{b}(t)}{b(t)} \iint_{\Omega(t)} z^m dx dy - b^2(t) \tilde{\tau} \int_{\partial\Omega(t)} \kappa \frac{\partial z^m}{\partial \mathbf{n}} ds \end{aligned}$$

where we have used (1.7) in the second equality, Green's theorem in the third one, and (1.8) in the last one. We have therefore come to the following theorem.

**Theorem 2.1.** *Suppose that  $\{\Omega(t)\}$  is a smooth family of simply connected domains.  $\{\Omega(t)\}$  is a solution of the initial value problem for the Hele–Shaw flow if and only if its complex moments satisfy*

$$\frac{d}{dt} \left[ \iint_{\Omega(t)} z^m dx dy \right] = -\frac{\dot{b}(t)}{b(t)} \iint_{\Omega(t)} z^m dx dy - b^2(t) \tilde{\tau} \int_{\partial\Omega(t)} \kappa \frac{\partial z^m}{\partial \mathbf{n}} ds. \quad (2.1)$$

**Proof.** We need only to show that if the moments satisfy equations (2.1), the corresponding  $\{\Omega(t)\}$  is a solution.

If  $p(x, y, t)$  denotes the solution to the Dirichlet problem for the Poisson equation (1.8), the previous argument shows that

$$-b^2(t) \int_{\partial\Omega(t)} z^m \frac{\partial p}{\partial \mathbf{n}} ds = -\frac{\dot{b}(t)}{b(t)} \iint_{\Omega(t)} z^m dx dy - b^2(t) \tilde{\tau} \int_{\partial\Omega(t)} \kappa \frac{\partial z^m}{\partial \mathbf{n}} ds.$$

This, combined with the assumption that

$$\begin{aligned} \int_{\partial\Omega(t)} z^m V_n ds &= \frac{d}{dt} \left[ \iint_{\Omega(t)} z^m dx dy \right] \\ &= -\frac{\dot{b}(t)}{b(t)} \iint_{\Omega(t)} z^m dx dy - b^2(t) \tilde{\tau} \int_{\partial\Omega(t)} \kappa \frac{\partial z^m}{\partial \mathbf{n}} ds \end{aligned}$$

gives

$$\int_{\partial\Omega(t)} z^m \left[ -b^2(t) \frac{\partial p}{\partial \mathbf{n}} - V_n \right] ds = 0 \quad m = 0, 1, 2, \dots$$

Since a continuous function  $[-b^2 \frac{\partial p}{\partial \mathbf{n}} - V_n]$  can be uniformly approximated by harmonic polynomials on  $\partial\Omega(t)$  this implies  $V_n = -b^2 \frac{\partial p}{\partial \mathbf{n}}$  on  $\partial\Omega(t)$ . Therefore,  $\{\Omega(t)\}$  solves the initial value problem, and the proof of theorem 2.1 is complete.  $\square$

**Corollary 2.2.** *The quantity*

$$b(t) \iint_{\Omega(t)} z^m dx dy$$

*is a constant of motion of the Hele–Shaw flows when  $\tilde{\tau} = 0$  for all nonnegative integer  $m$ 's, and when  $\tilde{\tau} \neq 0$  for  $m = 0$  and  $m = 1$ . In both cases, in particular, the centre of mass of the fluid domain is preserved by the motion.*

**Proof.** It is obvious from equation (2.1) that we only need to show that the above quantity is a constant of motion for  $m = 1$  when  $\tilde{\tau} \neq 0$ . To do this, it suffices to prove that the last integral of equation (2.1) is zero when  $m = 1$ . In fact, introducing the tangent angle  $\theta$  and arclength  $s$ , we obtain [31],

$$\int_{\partial\Omega(t)} \kappa \frac{\partial z}{\partial \mathbf{n}} ds = -i \int_{\partial\Omega(t)} \kappa [x'(s) + iy'(s)] ds = -i \int_{\partial\Omega(t)} \theta_s e^{i\theta} ds = 0.$$

This completes the proof of corollary 2.2.

Conservation of volume and centre of mass of the fluid serve as useful checks on numerical accuracy.

To simplify the moment problem (2.1), we divide it by  $Z^{m+1}$  for large  $|Z|$ . Summing the resulting equations, we obtain

$$\frac{d}{dt} \left[ \iint_{\Omega(t)} \frac{dx dy}{Z - z} \right] = -\frac{\dot{b}(t)}{b(t)} \iint_{\Omega(t)} \frac{dx dy}{Z - z} - b^2(t) \tilde{\tau} \int_{\partial\Omega(t)} \kappa \frac{\partial}{\partial \mathbf{n}} \left( \frac{1}{Z - z} \right) ds.$$

Rewriting the double and line integrals as complex integrals over  $\partial\Omega(t)$  yields

$$\frac{d}{dt} \left[ \frac{1}{2\pi i} \oint_{\partial\Omega(t)} \frac{z^*}{Z - z} dz \right] = -\frac{\dot{b}(t)}{b(t)} \frac{1}{2\pi i} \oint_{\partial\Omega(t)} \frac{z^*}{Z - z} dz - \frac{b^2(t)}{\pi i} \tilde{\tau} \oint_{\partial\Omega(t)} \frac{\kappa(z)}{(Z - z)^2} dz \quad (2.2)$$

for large  $|Z|$ , where the superscript  $*$  denotes complex conjugate. □

**Theorem 2.3.** *Suppose that  $\{\Omega(t)\}$  is a smooth family of simply connected domains.  $\{\Omega(t)\}$  is a solution of the initial value problem for the Hele–Shaw flow if and only if it satisfies equation (2.2) for large  $|Z|$ .*

### 2.2. Existence, uniqueness and regularity of solutions when $\tilde{\tau} = 0$

We now consider the zero surface tension case. We will establish the short time and global time existence, uniqueness, and regularity of solutions when the initial interface is analytic. We will also show that the initial value problem is ill-posed when  $b(t)$  is an increasing function.

We first summarize the basic properties of the Cauchy integral

$$\frac{1}{2\pi i} \oint_{\partial\Omega} \frac{z^*}{Z - z} dz \quad (2.3)$$

for a smooth closed Jordan curve  $\partial\Omega$ . This Cauchy integral defines two functions of  $Z$ ; one, denoted by  $U_e(Z)$ , is analytic outside  $\Omega$ , and the other, denoted by  $U_i(Z)$ , is analytic inside  $\Omega$ . These two functions are continuous up to the boundary  $\partial\Omega$ . On the boundary, their difference is given by the density in the Cauchy integral. More precisely, we have Plemelj’s formula:

$$U_e(Z) = Z^* + U_i(Z) \quad Z \in \partial\Omega. \quad (2.4)$$

Plemelj’s formula can be used to show that  $U_e(Z)$  can be analytically continued across  $\partial\Omega$  from outside if and only if  $\partial\Omega$  is an analytic curve [32].

We next use these properties to understand the regularity of the Hele–Shaw solutions. We first use the maximum principle for the Poisson equation to make the following observation.

**Lemma 2.4.** *If the initial value problem has a smooth solution  $\{\Omega(t)\}$  when  $\tilde{\tau} = 0$ ,  $\Omega(t)$  is contracting when  $\dot{b}(t) > 0$ , and expanding when  $\dot{b}(t) < 0$ .*

**Proof.** We only consider the case  $\dot{b}(t) > 0$ , and the other situation can be handled in the same way.

When  $\dot{b}(t) > 0$ ,  $p$  is subharmonic in view of (1.8). Moreover, it vanishes on  $\partial\Omega$ . It follows from the maximum principle that  $p$  reaches its maximum on  $\partial\Omega(t)$ , and that therefore,  $\frac{\partial p}{\partial \mathbf{n}} > 0$  on  $\partial\Omega(t)$  where  $\mathbf{n}$  is the outward normal vector to  $\partial\Omega(t)$ . This means that the domain  $\Omega(t)$  is contracting due to (1.7). The proof of lemma 2.4 is complete.  $\square$

Lemma 2.4 is not surprising in view of the fact that the top plate is lifted when  $\dot{b}(t) > 0$  and lowered when  $\dot{b}(t) < 0$ .

The integration of equation (2.2) when  $\tilde{\tau} = 0$  gives

$$\frac{1}{2\pi i} \oint_{\partial\Omega(t)} \frac{z^*}{Z - z} dz = \frac{b(0)}{b(t)} \frac{1}{2\pi i} \oint_{\partial\Omega(0)} \frac{z^*}{Z - z} dz \quad (2.5)$$

for large  $|Z|$ . When  $\dot{b}(t) > 0$ ,  $\Omega(t)$  is contracting;  $\Omega(t) \subset \Omega(0)$  strictly for  $t > 0$ . Since the left-hand side of equation (2.5) is analytic outside  $\Omega(t)$ , it is analytic in a domain containing  $\partial\Omega(0)$ . The second integral of the same equation is therefore analytic across  $\partial\Omega(0)$ . It follows from the analytic property mentioned previous to lemma 2.4 that  $\partial\Omega(0)$  is an analytic curve. In other words, the initial value problem has no smooth solution if the initial curve  $\partial\Omega(0)$  is not an analytic one.

When  $\dot{b}(t) < 0$ ,  $\Omega(t)$  is expanding. Repeating the same analysis, we can show that  $\partial\Omega(t)$  is always an analytic curve for  $t > 0$ . Therefore, we have established the following theorem.

**Theorem 2.5.** *In the case of zero surface tension, we have the following.*

(1) *When  $\dot{b}(t) > 0$ , the initial value problem for the Hele–Shaw flow has no smooth solution if  $\partial\Omega(0)$  is not an analytic curve.*

(2) *When  $\dot{b}(t) < 0$ ,  $\partial\Omega(t)$  must be an analytic curve for  $t > 0$  if  $\{\Omega(t)\}_{t \geq 0}$  is a smooth solution to the initial value problem.*

**Remark.** When  $\tilde{\tau} = 0$ , we may view the initial value problem for  $\dot{b}(t) < 0$  as the time-reversed process of that for  $\dot{b}(t) > 0$ . This is clear from equation (2.5). As a consequence, the first and second parts of theorem 2.5 are exactly two different statements of the same truth.

In the second part of this section, we will establish the existence and uniqueness of solutions to the initial value problem when the initial interface is analytic.

We first try to understand the physical meaning of the Cauchy integral. Rewriting (2.3) yields:

$$\begin{aligned} U(Z) &= \frac{1}{2\pi i} \oint_{\partial\Omega} \frac{z^*}{Z - z} dz \\ &= \frac{1}{\pi} \iint_{\Omega} \frac{1}{Z - z} dx dy \\ &= \left( \frac{\partial}{\partial X} - i \frac{\partial}{\partial Y} \right) \frac{1}{\pi} \iint_{\Omega} \log |Z - z| dx dy. \end{aligned}$$

The last double integral is the two-dimensional gravitational potential of the domain  $\Omega$  with a uniform density, and accordingly, the Cauchy integral is virtually the gravitational force at the point  $Z$ . It is natural to ask whether the gravitational information near infinity is enough to determine the shape of the domain  $\Omega$ . The answer is negative as different simply connected domains may give the same Cauchy integral [27]. We therefore seek a weaker form of the question as to what happens if we perturb a fixed gravitational force a little bit.

Can the resulting quantity be a gravitational force of another domain? Cherednichenko’s theorem says yes [11]. More precisely, given a function which is close to a Cauchy integral for a fixed analytic closed curve, then this function is a Cauchy integral of another closed curve which is near the fixed closed curve [11].

We next use Cherednichenko’s theorem to handle the existence and uniqueness of solutions. Suppose that the initial curve  $\partial\Omega(0)$  is an analytic curve with the Cauchy integral  $U_0(Z)$ . In view of equation (2.5), we consider

$$U(Z, t) = \frac{b(0)}{b(t)}U(Z, 0).$$

By Cherednichenko’s theorem, there exists a positive number  $\epsilon(\partial\Omega_0)$  which depends on the initial interface  $\partial\Omega_0$  such that  $U(Z, t)$  given by the above formula is a Cauchy integral of a unique closed analytic curve, say,  $\partial\Omega(t)$  if  $|\frac{b(0)}{b(t)} - 1| < \epsilon(\partial\Omega_0)$ . Since  $U(Z, t)$  smoothly depends on  $t$ , it can be checked that the velocity of  $\partial\Omega(t)$  continuously depends on time  $t$  and the arclength of  $\partial\Omega(t)$ . The proof can be found in [32]. By theorem 2.3,  $\{\Omega(t)\}$  solves the Hele–Shaw problem.

**Theorem 2.6.** *Given an initial simply connected domain  $\Omega_0$  with analytic boundary  $\partial\Omega_0$ , the initial value problem for the Hele–Shaw flow has one and only one analytic solution  $\{\Omega(t)\}_{t \geq 0}$  for small time  $t$ .*

Interestingly, we obtain a global time result if we restrict the behaviour of  $b(t)$ .

**Theorem 2.7.** *Given an initial simply connected domain  $\Omega_0$  with analytic boundary  $\partial\Omega_0$ , the initial value problem for the Hele–Shaw flow has one and only one analytic solution  $\{\Omega(t)\}_{t \geq 0}$  for all times if  $|\frac{b(0)}{b(t)} - 1| < \epsilon(\partial\Omega_0)$  for all times.*

### 2.3. Exact solutions with and without surface tension

In this section, we shall present some exact solutions. The purpose is to use them to illustrate how interfaces could behave. All solutions except the last one are without surface tension. We are interested in the case when  $b(t)$  is an increasing function with  $b(+\infty) = +\infty$ . Later, we shall present the computational results to show how a small surface tension might affect these exact solutions.

**2.3.1. Cusp formation.** We begin with an example to show that an interface can develop cusps when surface tension is zero. We consider a family of domains  $\{\Omega(t)\}$  which are the images of the unit disk  $|w| < 1$  under the conformal maps of the form  $f(w) = a_1(t)w + a_2(t)w^n$ . We may insist that  $a_1(t)$  be positive for each  $t$ . We want to see under what constraints on  $a_1(t)$  and  $a_2(t)$ ,  $\{\Omega(t)\}$  constitutes a Hele–Shaw solution.

For this goal, we calculate the Cauchy integral of  $\partial\Omega(t)$  for large  $|Z|$ .

$$\begin{aligned} \frac{1}{2\pi i} \oint_{\partial\Omega(t)} \frac{z^*}{Z - z} dz &= \frac{1}{2\pi i} \oint_{|w|=1} \frac{[a_1(t)]^* \frac{1}{w} + [a_2(t)]^* \frac{1}{w^n}}{Z - (a_1(t)w + a_2w^n)} [a_1(t) + na_2(t)w^{n-1}] dw \\ &= \frac{|a_1(t)|^2 + n|a_2(t)|^2}{Z} + \frac{a_1^n(t)[a_2(t)]^*}{Z^n}. \end{aligned}$$

By equation (2.5),  $\{\Omega(t)\}$  is a Hele–Shaw solution if and only if

$$\begin{aligned} |a_1(t)|^2 + n|a_2(t)|^2 &= \frac{b(0)}{b(t)} [|a_1(0)|^2 + n|a_2(0)|^2] \\ a_1^n(t)[a_2(t)]^* &= \frac{b(0)}{b(t)} a_1^n(0)[a_2(0)]^* \end{aligned}$$

and  $f(w, t) = a_1(t)w + a_2(t)w^n$  remains a conformal mapping on the unit disk  $|w| < 1$  for each time  $t$ . Since  $a_1(t)$  can be assumed to be always positive, it follows from the second equation that the argument of  $a_2(t)$  is preserved as time  $t$  varies. For convenience, we assume that  $a_2(t)$  is real. This simplifies the equations a bit, and we obtain

$$\begin{aligned} a_1^2(t) + na_2^2(t) &= \frac{b(0)}{b(t)}[a_1^2(0) + na_2^2(0)] \\ a_1^n(t)a_2(t) &= \frac{b(0)}{b(t)}a_1^n(0)a_2(0). \end{aligned}$$

The implicit function theorem can be used to show that these two equations can be solved for  $a_1$  and  $a_2$  as functions of  $t$  as long as  $a_1(t) \neq \pm na_2(t)$ , which is exactly the necessary and sufficient condition for the conformality of  $f(w, t) = a_1(t)w + a_2(t)w^n$ .

At the time when  $a_1(t) = \pm na_2(t)$ ,  $f_w$  has  $(n - 1)$  zeros on the unit circle. In other words, the interface will form  $(n - 1)$  symmetric cusps at the breaking. This breaking time, denoted by  $T_b$ , can easily be calculated by substituting  $a_1(t) = \pm na_2(t)$  into the above two equations. In this way, we find

$$\frac{b(0)}{b(T_b)} = \frac{(n^2 + n)^{\frac{n+1}{n-1}} |a_1^n(0)a_2(0)|^{\frac{2}{n-1}}}{n^{\frac{2n}{n-1}} [a_1^2(0) + na_2^2(0)]^{\frac{n+1}{n-1}}}.$$

**2.3.2. Topological changes.** In the second example, we show how a bubble can split into two different bubbles, within the conformal mapping approach. More precisely, we find an initial interface that will pinch and then fission into two circular interfaces of radius  $R$  centred at  $Z = \pm R$ . These two circular bubbles then separate, and shrink into their respective centres.

As the Hele–Shaw problem for  $\tilde{\tau} = 0$  is time reversible, it is more convenient to consider the backward problem. Starting with two circular interfaces with the same radius  $R$  centred at  $Z = -R$  and  $Z = R$ , we want to see what the interface will be at a later time in the case when  $b(t)$  is a decreasing function. The initial Cauchy integral can be easily calculated.

$$U(Z, 0) = \frac{1}{2\pi i} \oint_{|z+R|=R} \frac{z^*}{Z-z} dz + \frac{1}{2\pi i} \oint_{|z-R|=R} \frac{z^*}{Z-z} dz = \frac{R^2}{Z+R} + \frac{R^2}{Z-R}.$$

The equation of motion (2.5) gives the Cauchy integral at a later time.

$$U(Z, t) = \frac{b(0)}{b(t)} \left[ \frac{R^2}{Z+R} + \frac{R^2}{Z-R} \right]. \quad (2.6)$$

To determine the interface  $\partial\Omega(t)$  at time  $t$ , we introduce a Riemann conformal mapping  $Z = f(w, t)$  to map the unit disk  $|w| < 1$  onto the fluid domain  $\Omega(t)$ . We may insist that  $f(0, t) = 0$ . By the symmetry of the problem, there exists a positive  $w_0$  within the unit circle such that  $f(-w_0, t) = -R$  and  $f(w_0, t) = R$ . On the boundary, the Plemelj's formula gives

$$U(f(w), t) = [f(w)]^* + U_i(f(w)) = \hat{f} \left( \frac{1}{w} \right) + U_i(f(w)) \quad (2.7)$$

on  $|w| = 1$  where  $U_i(Z)$  is a function analytic in  $\Omega(t)$  and  $\hat{f}$  is the complex conjugate of  $f$ . The function  $\hat{f}$  is defined by  $\hat{f}(w) = [f(w^*)]^*$ , where the superscript  $*$  denotes complex conjugate. It is easy to check that the domains of analyticity for  $f$  and  $\hat{f}$  are symmetric

about the real axis. Since the left-hand side has two simple poles at  $w = -w_0$  and  $w = w_0$  with the same residue in view of (2.6), so is  $\hat{f}(\frac{1}{w})$  and therefore,

$$\hat{f}\left(\frac{1}{w}\right) = \frac{\alpha}{w + w_0} + \frac{\alpha}{w - w_0} + g(w) \tag{2.8}$$

where  $\alpha$  is a constant which can be shown to be real and  $g(w)$  is analytic in the unit disk. As  $\hat{f}(\frac{1}{w})$  is analytic outside the unit disk and vanishes at infinity, it follows from equation (2.8) that so is  $g(w)$ . Therefore,  $g(w)$  is identically zero. Recovering  $f(w)$  from equation (2.8), we obtain

$$f(w) = \frac{2\alpha w}{1 - w_0^2 w^2}. \tag{2.9}$$

The coefficients  $\alpha$  and  $w_0$  are determined by the conditions that  $f(w_0) = R$  and that the residues of both sides of equation (2.7) must be the same. In this way, we obtain,

$$\alpha = \frac{1 - w_0^4}{2w_0} R \quad w_0 = \sqrt{\frac{b(0)}{b(t)} - \sqrt{\left[\frac{b(0)}{b(t)}\right]^2 - 1}}. \tag{2.10}$$

In the  $X, Y$  coordinates, the interface given by (2.9) has the following algebraic expression

$$(X^2 + Y^2)^2 = \frac{4\alpha^2 X^2}{(1 - w_0^2)^2} + \frac{4\alpha^2 Y^2}{(1 + w_0^2)^2}.$$

The same interface was also found by Richardson [25, 34] when he tried to understand how an expanding bubble interacts with a straight wall. The technique used here is also due to Richardson. Note, however, that velocities diverge to infinity at the time of pinching, hence making it difficult to compute even at times earlier than the time of the interface break-up.

**2.3.3. Annular fluid domains.** Finally, we will present a Hele–Shaw solution with a doubly connected fluid domain. This domain  $\Omega(t)$  will be an annulus with  $r(t)$  and  $R(t)$  as the interior and exterior radii respectively. We assume that we have gas inside and outside the annulus, and that both regions have the same constant pressure. In practice, this could be achieved by connecting each gas region to the atmosphere. For convenience, we also suppose the annulus to be centred at the origin.

Accordingly, the Dirichlet problem for the Poisson equation (1.8) becomes

$$\Delta p = \frac{\dot{b}(t)}{b^3(t)} \quad \text{in } \Omega(t)$$

$$p = \frac{\tilde{\tau}}{R} \quad \text{on } x^2 + y^2 = R^2 \tag{2.11}$$

$$p = -\frac{\tilde{\tau}}{r} \quad \text{on } x^2 + y^2 = r^2. \tag{2.12}$$

The unique solution  $p$  can be solved explicitly, and we find

$$p = \frac{1}{4} \frac{\dot{b}(t)}{b^3(t)} [x^2 + y^2] + \alpha \log \sqrt{x^2 + y^2} + \beta.$$

The coefficients  $\alpha$  and  $\beta$  are determined by the boundary conditions (2.11) and (2.12). These together with the kinematic condition (1.7) give the evolution of  $R(t)$  and  $r(t)$

$$\frac{dR}{dt} = -\frac{\dot{b}(t)}{b(t)} \left[ \frac{R}{2} + \frac{R^2 - r^2}{4R \log \frac{r}{R}} \right] + b^2(t) \tilde{\tau} \frac{\frac{1}{R} + \frac{1}{r}}{R \log \frac{r}{R}} \tag{2.13}$$

$$\frac{dr}{dt} = -\frac{\dot{b}(t)}{b(t)} \left[ \frac{r}{2} + \frac{R^2 - r^2}{4r \log \frac{r}{R}} \right] + b^2(t) \bar{\tau} \frac{\frac{1}{R} + \frac{1}{r}}{r \log \frac{r}{R}}. \quad (2.14)$$

Both terms on the right-hand side of the first equation are negative for  $0 < r < R$ . As a result,  $R(t)$  is always decreasing with time  $t$ .

It is not difficult to check that equations (2.13) and (2.14) are equivalent to the two equations:

$$\frac{d}{dt} [R^2 \log R^2 - r^2 \log r^2] = -\frac{\dot{b}(t)}{b(t)} [R^2 \log R^2 - r^2 \log r^2] - 4b^2(t) \bar{\tau} \left( \frac{1}{R} + \frac{1}{r} \right) \quad (2.15)$$

$$\frac{d}{dt} [R^2 - r^2] = -\frac{\dot{b}(t)}{b(t)} [R^2 - r^2]. \quad (2.16)$$

It is interesting that equations (2.15) and (2.16) are also easily obtained by following the evolution of the global quantities:

$$\iint_{\Omega(t)} \log \sqrt{x^2 + y^2} \, dx \, dy \quad \iint_{\Omega(t)} 1 \, dx \, dy$$

as in the derivation of equations of motion for simply connected fluid domains. The first integral gives the gravitational information at the origin, and it is needed to detect the interior circle.

By basic results of ordinary differential equations, equations (2.13) and (2.14) have a unique solution  $R(t)$  and  $r(t)$  so long as  $0 < r < R$ . In the relevant time interval, we integrate equations (2.15) and (2.16) to obtain

$$R^2(t) \log R^2(t) - r^2(t) \log r^2(t) = \frac{b(0)}{b(t)} [R^2(0) \log R^2(0) - r^2(0) \log r^2(0)] - \frac{4\bar{\tau}}{b(t)} \int_0^t \left[ \frac{1}{R(\lambda)} + \frac{1}{r(\lambda)} \right] b^3(\lambda) \, d\lambda \quad (2.17)$$

$$R^2(t) - r^2(t) = \frac{b(0)}{b(t)} [R^2(0) - r^2(0)]. \quad (2.18)$$

We next consider the cases when  $\bar{\tau} = 0$  and  $\bar{\tau} \neq 0$  separately.

When  $\bar{\tau} = 0$ , we will show that  $R(t)$  and  $r(t)$  exist for all positive times, and that the annulus will shrink to a circle as  $t \rightarrow +\infty$ . It follows from (2.13) and (2.14) that  $R(t)$  is decreasing and  $r(t)$  increasing with time  $t$ . In view of (2.18),  $R(t)$  and  $r(t)$  can coalesce only at  $t = +\infty$ . This shows that  $R(t)$  and  $r(t)$  exist for all nonnegative  $t$ . Eventually, the annular fluid domain will shrink into a circle. The radius  $R_\infty$  of this terminal circle can be found by dividing (2.17) by (2.18) and letting both  $R(t)$  and  $r(t)$  go to  $R_\infty$ . In this way, we obtain

$$1 + 2 \log R_\infty = \frac{R^2(0) \log R^2(0) - r^2(0) \log r^2(0)}{R^2(0) - r^2(0)}.$$

Applying the mean value theorem to the right-hand side, we see that  $R_\infty$  is between  $R(0)$  and  $r(0)$  as expected.

When  $\bar{\tau} \neq 0$ , we will see that  $r(t)$  will vanish in a finite time. We will justify our claim by contradiction. Suppose that  $r(t)$  does not vanish in a finite time. By equation (2.18),  $R(t)$  and  $r(t)$  will not coalesce in a finite time. As a consequence, the solutions  $R(t)$  and  $r(t)$  always satisfy  $0 < r(t) < R(t)$  and thus, they exist for all time  $t > 0$ . When time is large,  $R(t)$  and  $r(t)$  are nearly equal and therefore the first term of (2.17) is small. The second term of the same equation is also small. Therefore, we obtain a contradiction to equation (2.17) since the last term is bounded away from zero when time is large. We have

thus shown that  $r(t)$  will vanish in a finite time. Right at this moment, it can be checked that the fluid velocity blows up at the centre.

### 3. Numerical simulations

#### 3.1. Formulation and numerical methods

To simulate the motion of a patch of fluid we reformulate the equations of motion in terms of boundary integrals—a standard approach to computing Hele–Shaw flows [33, 17]. This formulation expresses the velocity inside the bubble, and of the interface itself, solely in terms of the interface position  $z(\alpha, t)$ . While a boundary integral representations would usually only apply for a harmonic pressure, the pressure in system (1.5) differs from being harmonic by the simple particular solution  $\bar{p}$ , which is explicitly removed. This approach is identical to the representation technique used by Baker and Shelley [4] in their study of the contour dynamics problem.

The velocity of the fluid is thus decomposed into an explicit term from the particular solution  $\bar{p}$ , and that arising from the harmonic remainder, represented as a dipole distribution along  $\partial\Omega$ . In this formulation, the evolution equations for the complex interface position  $z(\alpha, t)$ , where  $\alpha$  is the Lagrangian variable and  $0 \leq \alpha \leq 2\pi$ , are given by

$$z_t^*(\alpha, t) = -\frac{\dot{b}}{2b}z^*(\alpha, t) - \frac{\gamma(\alpha, t)}{2z_\alpha(\alpha, t)} + \frac{1}{2\pi i}P \int_0^{2\pi} \frac{\gamma(\alpha', t)}{z(\alpha, t) - z(\alpha', t)} d\alpha'. \quad (3.1)$$

The superscript  $*$  denotes complex conjugation, and the  $P$  denotes a principal value integral. The *sheet strength*  $\gamma$  is determined as the solution of the Fredholm integral equation of the second kind,

$$\frac{\gamma(\alpha, t)}{2} - \text{Re} \left\{ \frac{z_\alpha(\alpha, t)}{2\pi i} P \int_0^{2\pi} \frac{\gamma(\alpha', t)}{z(\alpha, t) - z(\alpha', t)} d\alpha' \right\} = b^2 \tilde{\tau} \kappa_\alpha - \frac{\dot{b}}{2b} \text{Re}\{z^* z_\alpha\} \quad (3.2)$$

solved under the constraint that

$$\int_0^{2\pi} d\alpha \gamma(\alpha, t) = 0.$$

A short derivation of these equations of motion is given in the appendix.

The choice of numerical method is dictated by the absence or presence of surface tension. If  $\tilde{\tau} = 0$ , we solve the above system directly, using Krasny filtering [18] to control the spurious growth of rounding-off errors, spectrally accurate spatial discretizations [29], and a preconditioned GMRES iteration [26] to solve the integral equation. Time stepping is accomplished by a third-order Adams–Bashforth method. When  $\tilde{\tau} > 0$ , we use the small-scale decomposition (SSD) approach developed by Hou *et al* [17], coupled to a second-order Adams–Bashforth scheme, to avoid the third-order time-step constraints accompanying surface tension. Applying the SSD involves reformulating the equations of motion in terms of the interface’s length  $L$  and its tangent angle  $\theta$ , and evolving these new variables. This new formulation leaves a first-order CFL constraint, satisfied by an automatic time-step control in our time-stepping implementation. These numerical methods were thoroughly discussed by Hou *et al* [17].

The correctness of these implementations was checked in a number of ways. This included comparing the computed results with cases where the solution to the integral equation and resulting velocity could be found analytically, and also comparing with exact dynamical solutions (as found in the previous section). Agreement of the simulated evolution was also verified with solutions of the linearized equations for small amplitude perturbations

of a shrinking circle. Finally, conformance with the convergence estimates of our numerical method was also checked, i.e. infinite order in space, and  $O(\Delta t^2)$  in time for  $\tilde{\tau} > 0$ , and  $O(\Delta t^3)$  in time for  $\tilde{\tau} = 0$ .

### 3.2. Results

We have computed a number of different cases which illustrate and expand upon the results of sections 1 and 2. First, we examine pattern formation through the full nonlinear development of the Saffman–Taylor instability, and examine the effect of varying surface tension. Secondly, we examine the inclusion of surface tension on initial data that in the absence of surface tension would split from a single domain into two circles.

*3.2.1. Pattern formation.* The distinctive pattern formation found in our system is illustrated by considering evolution from a multimode perturbation of the unit circle, for various surface tensions, including  $\tilde{\tau} = 0$ . Here we take  $b(t) = e^t$ . The initial data is

$$\begin{aligned}x(\alpha, 0) &= r(\alpha) \cos \alpha \\y(\alpha, 0) &= r(\alpha) \sin \alpha\end{aligned}$$

with  $r(\alpha) = 1 + 0.02(\cos 3\alpha + \sin 7\alpha + \cos 15\alpha + \sin 25\alpha)$ .

This initial data is seen in the upper left box of figures 2–4, which show the evolution for the three surface tensions  $\tilde{\tau} = 2 \times 10^{-4}$ ,  $10^{-4}$ , and  $\frac{1}{2} \times 10^{-4}$ . All three simulations use an initial time-step of  $\Delta t = 10^{-4}$  with a spatial resolution of 4096 points. This was found to be sufficient in all cases to maintain temporal resolution, and to keep the active part of the Fourier spectrum (in  $\alpha$ ) beneath the Nyquist frequency.

We describe the behaviour in detail for the  $\tilde{\tau} = 10^{-4}$  simulation, shown in figure 3. The linear stability analysis gives that there are initially 70 unstable modes, with the most rapidly growing initial mode at  $k_{\max} = 41$ . The evolution goes through three distinct stages. First, the initial valleys deepen, exposing their structure. Indeed, the number of intrusions seen at  $t = 0.65$  is on the order of the number of initial indentations. It is soon apparent that each of these deepening valleys is a Saffman–Taylor finger penetrating into the liquid, with the deeper initial valleys tending to produce the larger fingers. The tips of the ‘fjords’ separating the fingers are relatively pinned, moving inwards much more slowly. The larger fingers also become thicker at the centre and so acquire rounder shapes, similar to those seen in gap gradient Hele–Shaw experiments (see [36, 6, 30]). As is typical in Hele–Shaw systems, there is a competition amongst these fingers, and the smaller fingers eventually flatten out and disappear completely. At  $t = 1.15$ , there are only nine long ‘fjords’ of liquid remaining, each associated with the deeper initial valleys. This is the first stage—the rapid ramification of the interface, via a Saffman–Taylor instability, through the penetration of multiple fingers of gas into the fluid.

In the next stage, the larger fingers continue their inward flight, but the previously pinned ends of the fjords begin to draw in very rapidly, and the interface begins to deramify. This is clearly seen in the last three boxes of the figure. This is itself not a gentle process. Droplets are attached to the ends of the fjords, and as the fjord shortens, these droplets tend to circularize. This creates thin necks of fluid where the droplets attach to the bulk, and it appears as though they might ‘pinch off’, and separate the droplet of fluid from the body. This would constitute a flow singularity in our model equations. It does not appear that such a singularity occurs in these simulations, although we do believe that it is likely to occur with harder driving, or with different initial conditions. We will return to this point at the end of the section.

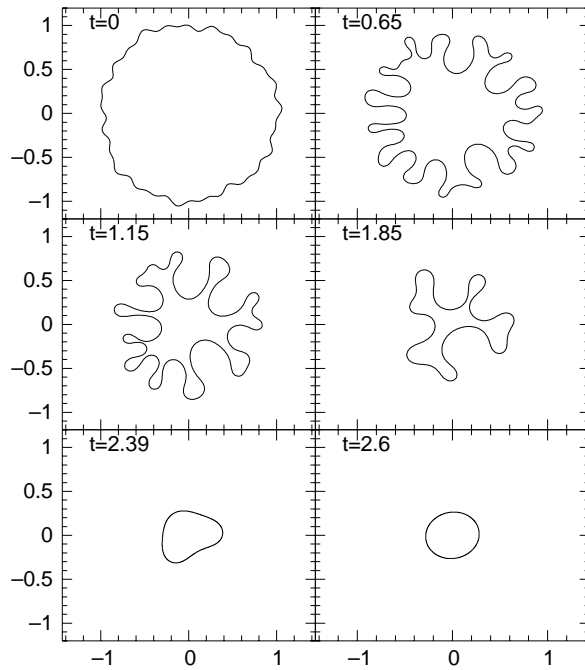


Figure 2. Simulation of the bubble with  $\bar{\tau} = 2 \times 10^{-4}$ .

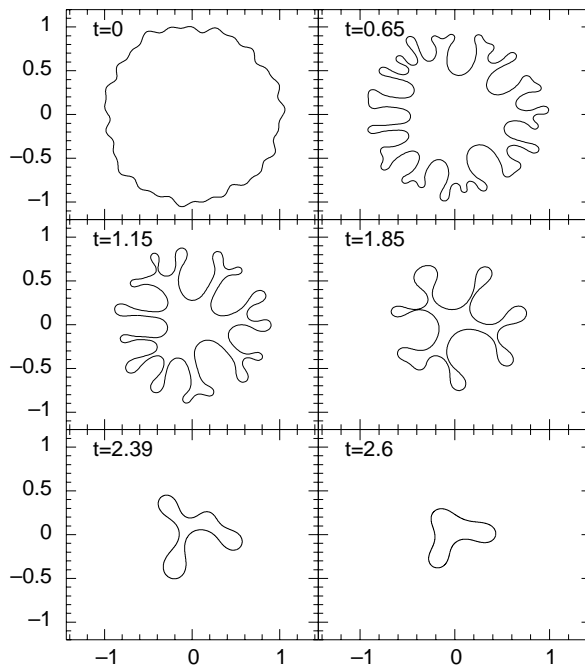
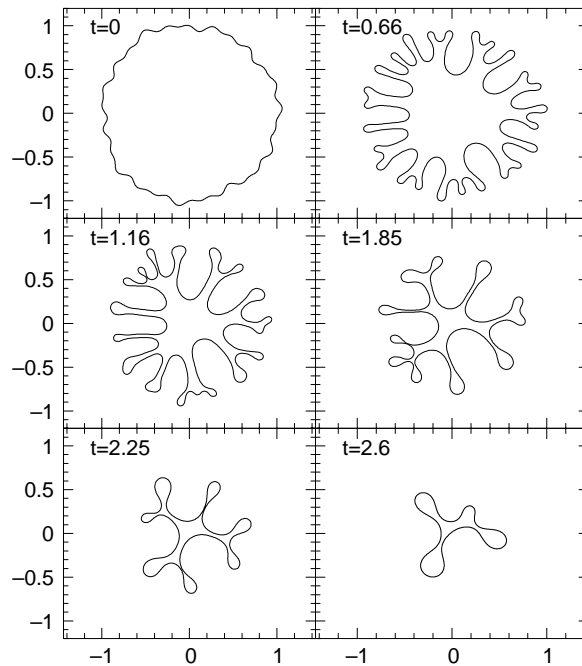


Figure 3. Simulation of the bubble with  $\bar{\tau} = 10^{-4}$ .



**Figure 4.** Simulation of the bubble with  $\tilde{\tau} = \frac{1}{2} \times 10^{-4}$ .

In the final stage, the interface completely deramifies, and relaxes to a shrinking circle. This is consistent with the linear analysis, and with experimental observation in the gap gradient case. It has been confirmed in gap gradient experiments that finger growth is only observed for interfacial velocities above a certain threshold (see [36]). Here, the gap width is growing exponentially ( $b(t) = e^t$ ), and the average speed of interface is proportional to  $\frac{1}{\sqrt{b(t)}} = e^{-t/2}$ —a decreasing speed.

For the larger surface tension  $\tilde{\tau} = 2 \times 10^{-4}$  (figure 2), the number of initially unstable modes decreases to 50, with  $k_{\max} = 29$ . This has a yet stronger smoothing effect on the shape of the interface. The smaller fingers die out more quickly, and by the time  $t = 0.65$  they are practically absent. The large fingers become shorter and thicker leaving more fluid closer to the centre rather than spread in ‘fjords’. Again, there is no time at which any of the fingers would become so thin that we could believe a pinching might occur. The interface evolves much faster towards a simpler form and by  $t = 1.85$  there are only four fingers left. When  $t = 2.6$  the interface acquires a nearly circular shape.

Figure 4 shows the simulation for the smallest surface tension  $\tilde{\tau} = \frac{1}{2} \times 10^{-4}$ , for which there are approximately 100 initially unstable modes, with  $k_{\max} = 58$ . Now the small fingers do not smooth out, but rather become longer and live for a more extended duration, and the fjords which endure for most of the simulation are generally much thinner. Also, the main body of fluid occupies a significantly smaller area yielding an impression that from time  $t \approx 0.9$  the blob is actually a network of fjords. Despite going through several ‘near-pinching’ situations the network finally reduces to a circular shape by  $t = 3.2$ .

As usual, the ramification of the interface depends on the surface tension—the smaller the surface tension, the more structured the interface. To explore this in more detail, we consider the index  $I(t) = L(t)/\sqrt{4\pi \text{Area}(\Omega(t))}$ —that is, the ratio of the length of the

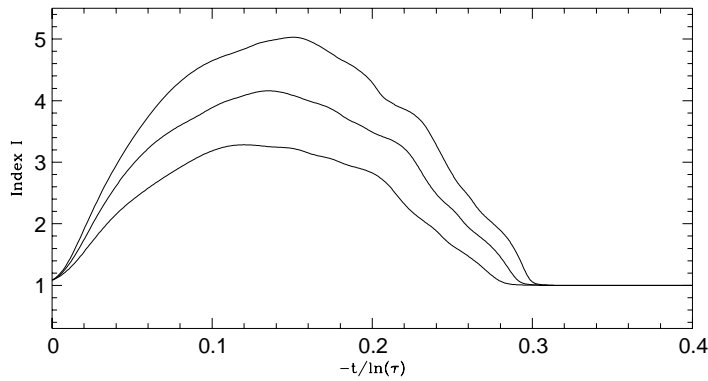


Figure 5. The index  $I(t)$  as a function of  $t$ .

interface to the circumference of a circle having the same area as the cross section of the bubble. Figure 5 shows  $I(t)$  for each of the three runs described above. Linear theory suggests that we should rescale time as  $s = -t/\ln \tilde{\tau}$  (the scaling of time to reach maximum amplitude, before the linear instability saturates), and  $I$  is plotted to good effect on this rescaled time. This index reflects well the departure from a perfect circle, which has index  $I \equiv 1$ , and also the increase in complexity of the interface as  $\tilde{\tau}$  is decreased (greater maximum  $I$  accompanies decreased  $\tilde{\tau}$ ). The eventual recircularization of the bubble is also evident. While linear theory suggested a time rescaling, it did not give a rescaling in the amplitude of  $I$  that collapsed these curves onto one another. It appears from direct examination of the data that halving the surface tension led to an arithmetic increase in  $I$ . That is, a logarithmic dependence on  $\tilde{\tau}$ . Of course, this putative behaviour is ‘observed’ on only three data points.

Finally, we include a simulation for evolution with  $\tilde{\tau} = 0$ . Using  $N = 4096$  points, figure 6 shows the initial data (the outer graph) and the interface, as it propagates inwards, at several times up to  $t = 0.04$ . Over this short time, the interface begins to sharpen, and the spatial Fourier spectrum broadens rapidly, quickly exhausting the available resolution. In comparison with the above simulations, this experiment illustrates the strong smoothing effect of surface tension. When  $\dot{b} > 0$  and  $\tilde{\tau} = 0$ , so that all length-scales are unstable, we expect the formation of interfacial cusps in finite time to be a *generic* feature of the bubble evolution, as it is for more standard Hele–Shaw problems without surface tension [28]. If the appearance of such a cusp is an imminent event for this flow, this would explain the rapid broadening of the Fourier spectrum.

**3.2.2. The effect of surface tension on a fissioning interface.** In section 2 we showed that in the absence of surface tension an interface, described by equations (2.9), (2.10) with  $\omega_0 = \frac{1}{2}$ ,  $R = 1$  and  $b(t) = e^t$ , could bifurcate into two shrinking circles. What is the effect of surface tension on this ‘topological singularity’?

Figure 7 shows evolution from this data, with  $\tilde{\tau} = 2 \times 10^{-4}$ . In the absence of surface tension this interface fissions into two circles, centred at  $(1, 0)$  and  $(-1, 0)$ , when  $b(t_f) = \frac{17}{8}b(0)$ , or  $t_f \approx 0.75$ . The broken curves show the  $\tilde{\tau} = 0$  solution at each time. This simulation uses the initial time-step  $\Delta t = 2 \times 10^{-4}$  and an initial spatial resolution of  $N = 2048$  points, which was increased later to 4096 and then to 8192. We remark that  $N = 2048$  points were sufficient to maintain spatial resolution throughout the simulation.

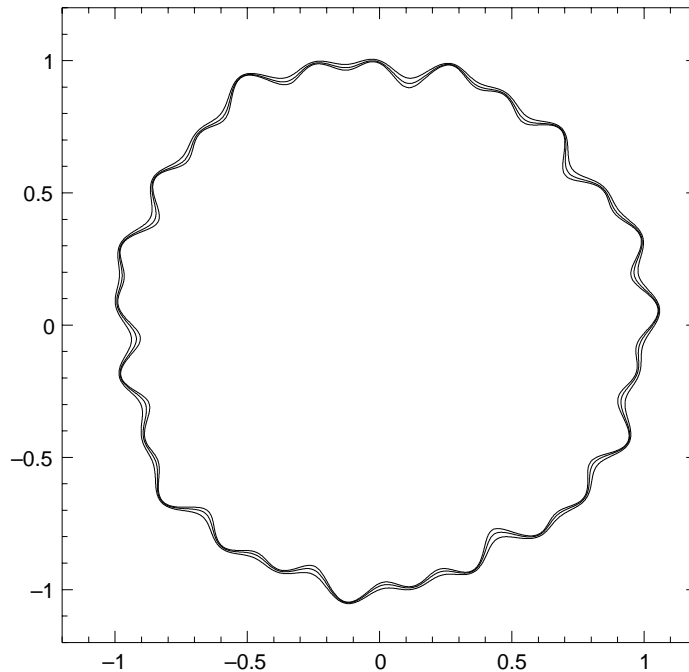


**Figure 6.** Simulation of the bubble with  $\tilde{\tau} = 0$ .

However, at late times (say  $t = 3.0$  in figure 7) disparate sections of the interface approach one another, which leads to loss of accuracy in the quadrature of the velocity integral (see Baker and Shelley [3] for an analysis). While adaptive quadrature methods can be used to ameliorate this error, we did not do so; instead, we took the easier, but computationally more expensive approach of simply increasing the global resolution.

The presence of surface tension completely changes the ultimate motion of the interface. Initially, the interface (see figure 7) behaves similarly to the  $\tilde{\tau} = 0$  evolution. But by  $t = t_f$  the smoothing effect of surface tension is clear. The  $\tilde{\tau} = 0$  interfacial cusp is altered to a flattened, more slowly advancing front. (This is very similar to behaviour seen in Dai *et al* [13] in their study of the effect of surface tension on cusp formation (but with no fissioning) on an expanding bubble in the Hele–Shaw cell.) Away from the fission region, fidelity is maintained surprisingly well to the zero surface tension solution. Consequently, as the fissioned circles (again, broken curves) recede away from each other (remaining centred at  $(\pm 1, 0)$ ), the flattened front is drawn out into a dumbbell shape, with two masses of fluid connected by a thinning neck of fluid having a central bulge. By  $t = 3.0$ , this central bulge has disappeared, and the bubble shape begins to differ strongly everywhere from the fissioned circles.

Figure 8 shows the effect of reducing  $\tilde{\tau}$ , by a factor of 2, to  $10^{-4}$ . Aside from their time of appearance, the basic features of this simulation remain the same as for the larger surface tension simulation, i.e. removal of the fissioning singularity, the evolution to a dumbbell shape, with a thin connecting neck between two larger fluid masses. At the fission time  $t_f$ , the flat front that has replaced the cusp is of about the same width as that for the  $\tilde{\tau} = 2 \times 10^{-4}$  simulation; the most noticeable difference is the small dimple that becomes the pinned end of a very short fjord at the side of what is apparently a finger propagating

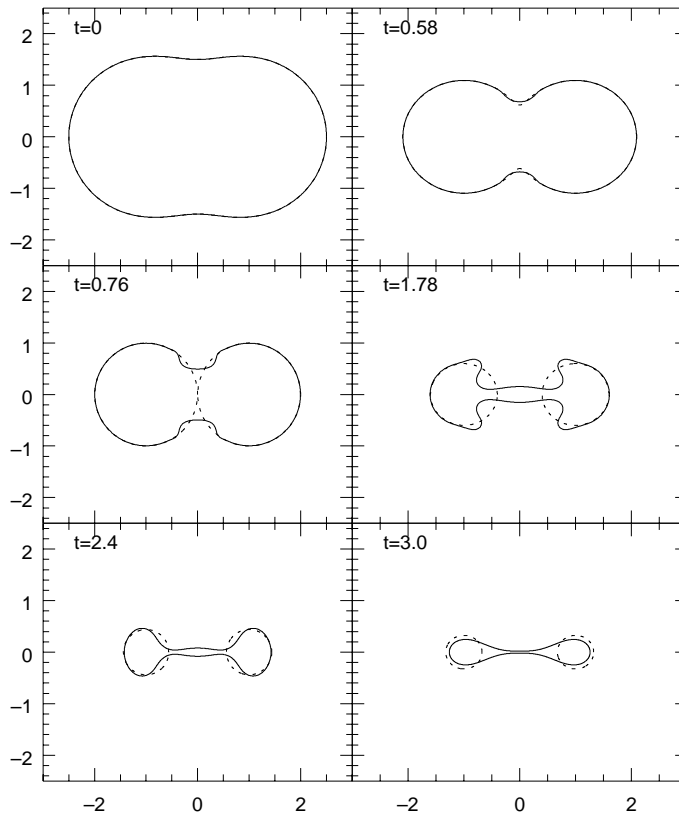


Figure 7. Simulation of the bubble with  $\tilde{\tau} = 2 \times 10^{-4}$ .

into the circle. In contrast to the  $\tilde{\tau} = 2 \times 10^{-4}$  simulation, at  $t = 3.0$  there is still a region of strong agreement between the bubble shape and the fissioned circles. Indeed, the bubble resembles very much that for the larger surface tension at the earlier time  $t = 2.4$ . At  $t = 3.47$ , the bulge of fluid in the neck is again lost, and the similarity is strong with the  $\tilde{\tau} = 2 \times 10^{-4}$  simulation at  $t = 3.0$ .

Unfortunately, we were unable to reduce the surface tension any further, due to the growth of rounding-off errors in the most unstable wavelengths. Figure 9 shows the early time evolution (up to  $t = 0.59 < t_f$ ) for  $\tilde{\tau} = \frac{1}{2} \times 10^{-4}$ . The simulation breaks down soon thereafter. Small ripples develop in the interface around  $x = 0$  and develop rapidly into intruding fingers. These small ripples are characteristic of (linear) growth rates of the most unstable length-scales being large enough to inflate initial rounding-off errors to  $O(1)$  size on this timescale (see Dai and Shelley [14] for a study of the interaction of noise and surface tension in a standard Hele–Shaw flow). Examination of the Fourier spectrum confirms this interpretation. This spurious behaviour is an artefact of the finite precision of the simulation, and its removal would require an increase in the precision (here, 64 bits—double precision).

What happens beyond  $t = 3.0$  for  $\tilde{\tau} = 2 \times 10^{-4}$ , and  $t = 3.47$  for  $\tilde{\tau} = 10^{-4}$ ? We do not know. At this point, with the collapse of the central bulge, we find the onset of a strong symmetry breaking instability, that causes the two sides of the neck in the centre to ‘slip’ in opposite directions, breaking the up/down, left/right symmetry of the interface. Such symmetries are preserved by the equations of evolution if present in the initial data.

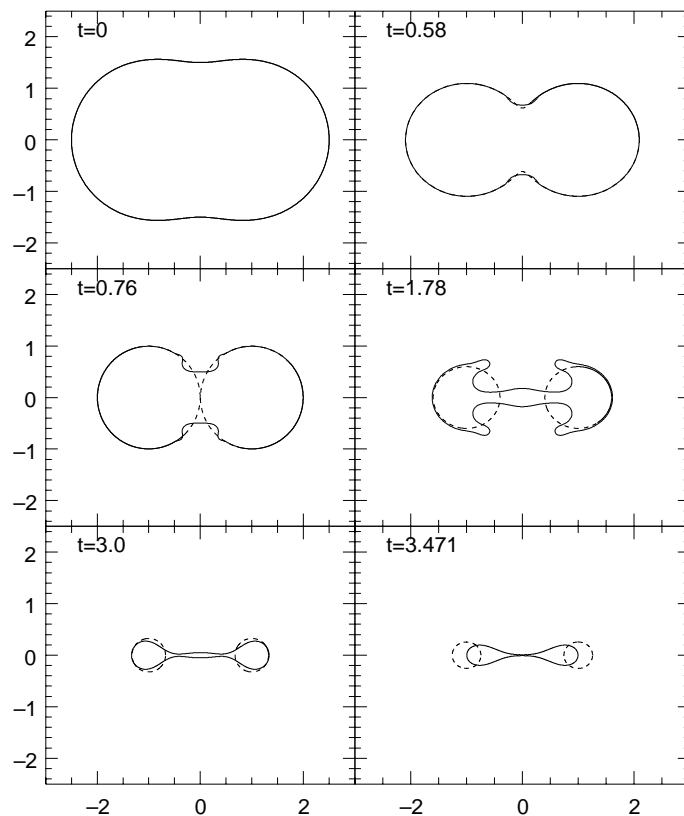


Figure 8. Simulation of the bubble with  $\tilde{\tau} = 10^{-4}$ .

As we did not explicitly enforce such symmetries in our simulation, we must conclude that our simulation has lost accuracy.

One reasonable expectation for the ensuing bubble behaviour is that the two outer droplets merge together, and the entire shape circularizes (as in the previous section). However, we conjecture that if the above instability was suppressed, this process would be abbreviated by the finite time collision of the opposing interfaces in the neck region—a topological singularity—perhaps signalling an incipient break-up of the bubble. Figure 10 shows the width of the bubble at  $x = 0$  for the  $\tilde{\tau} = 10^{-4}$  simulation. It does appear that this width is decreasing rapidly towards zero, in support of our conjecture, but we consider our evidence far from definitive. Examination of quantities that should diverge in such an event (i.e.  $\kappa_s$  on the interface, see [16]) do not as yet show strongly singular behaviour.

Bubble break-up for a patch of fluid in the regular Hele–Shaw problem ( $\dot{b} = 0$ ) has recently been considered by Almgren [1], who numerically studied the evolution of a bubble from dumbbell-shaped initial data. Almgren found strong evidence for such finite-time pinching of the neck. Perhaps a symmetry breaking instability such as we observe is not operative in this case. Analytically, such behaviour in Hele–Shaw flows has been studied extensively in the context of lubrication theory, in which the neck is considered to be slender. A companion study to Almgren [1] using lubrication theory is given by Almgren *et al* [2].

A lubrication approximation for flow in a thin neck for the present problem, with

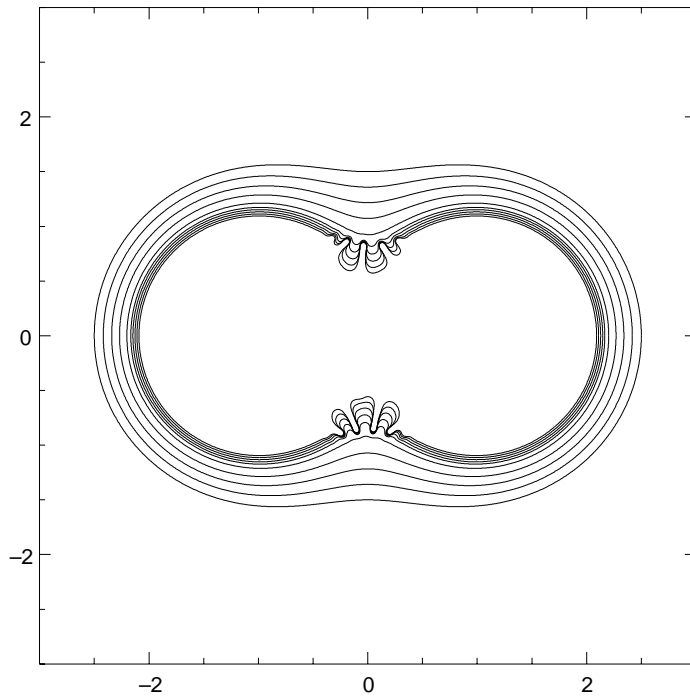


Figure 9. Simulation of the bubble with  $\tilde{\tau} = \frac{1}{2} \times 10^{-4}$ .

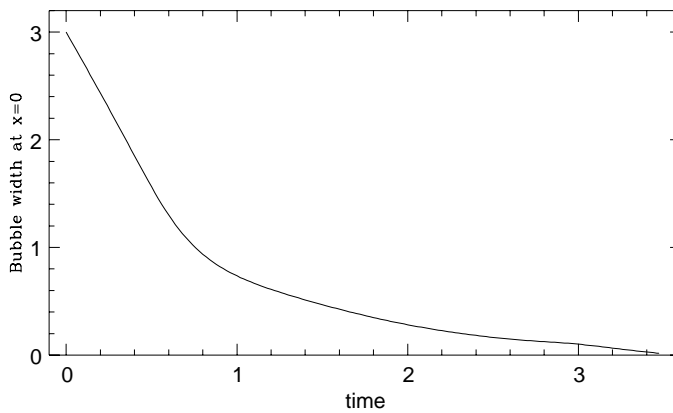


Figure 10. Bubble width at  $x = 0$  for  $\tilde{\tau} = 10^{-4}$ .

up/down symmetry imposed, has been found by Mary Pugh (private communication). In this approximation, the thickness of the neck is governed by the PDE

$$h_t = -b^2 \tilde{\tau} (h h_{xxx})_x - \frac{\dot{b}}{b} h \tag{3.3}$$

where  $h$  is one-half of the neck width. After the change of variables  $\tilde{h} = b(t)h(x, t)$  this becomes

$$\tilde{h}_t = -b \tilde{\tau} (\tilde{h} \tilde{h}_{xxx})_x \tag{3.4}$$

where the factor  $b\tilde{\tau}$  can be absorbed into a rescaled time. This is then identical to the lubrication approximation for a thin neck in the regular Hele–Shaw problem with constant gap width. This PDE and its variants have been studied extensively [12, 16, 7, 2], and there is a significant amount of numerical evidence indicating that such equations can acquire a pinching singularity— $h \downarrow 0$ —in a finite time. However, it is also the case that the appearance of such singularities can depend very much on initial and boundary conditions, or on the presence of additional physics that give large-scale instability. We recognize however that approaching a pinching singularity is beyond the asymptotic range used in derivation of our original system, as it is for standard Hele–Shaw flow, and so may not be physically relevant.

#### 4. Conclusion

In this paper, we have studied the dynamics of a fluid bubble in a Hele–Shaw cell with time-dependent gap-width. For a lifting plate, we identify a basic instability (a version of the Saffman–Taylor instability) in a Darcy’s law that is modified to account for the plate time dependence. Analytically, we establish conditions for the existence, uniqueness and regularity of solutions when the surface tension is zero. We also construct some exact analytic solutions, both with and without surface tension. These solutions illustrate some of the possible behaviours of the system, such as cusp formation and bubble fission. Numerically, we study the distinctive pattern formation resulting from this Saffman–Taylor instability, and study the effect of surface tension on a bubble evolution that in the absence of surface tension would fission. On the latter, we find some evidence of a topological singularity when surface tension is included, but it seems to be associated with fission of a thin neck of fluid, rather than with the collision of incipient cusps.

#### Acknowledgments

We thank Ray Goldstein, John Lowengrub, Mary Pugh, and Andy Woods for important conversations. MJS acknowledges support from Department of Energy grant DE-FG02-88ER25053, National Science Foundation grants DMS-9396403 (PYI) and DMS-9404554, and the Exxon Educational Foundation. FRT acknowledges support from National Science Foundation grant DMS-9622810 and The Ohio State University through a Seed Grant award. An mpeg movie of the simulation of pattern formation shown in figure 3 can be accessed at the web site <http://math.nyu.edu/faculty/shelley>.

#### Appendix. Integral formulation

The pressure can be given as  $p = \bar{p} + \tilde{p}$  where  $\bar{p} = \frac{1}{4} \frac{\dot{b}}{b^3} (x^2 + y^2)$  is the ‘free-space’ radial solution and  $\tilde{p}$  satisfies the Laplace’s equation.  $\tilde{p}$  can be represented as a dipole distribution with strength  $\rho$  along  $\partial\Omega$ . It is convenient to work in complex variables where  $\eta = x + iy$  is a point in  $\Omega$  and  $z(\alpha, t) = x(\alpha, t) + iy(\alpha, t)$ ,  $0 \leq \alpha \leq 2\pi$  denotes the boundary  $\partial\Omega$ . The complex velocities inside  $\Omega$  due to  $\bar{p}$  and  $\tilde{p}$  are

$$Q = \bar{Q} + \tilde{Q} = u + iv. \quad (\text{A.1})$$

$\bar{Q}$  is given by

$$\bar{Q} = -b^2(\bar{p}_x + i\bar{p}_y) = -\frac{\dot{b}}{2b}(x + iy) = -\frac{\dot{b}}{2b}\eta \quad (\text{A.2})$$

and  $\tilde{Q}$  is expressed as that induced by a vortex sheet along  $\partial\Omega$ , or

$$\tilde{Q}^* = -b^2(\tilde{p}_x - i\tilde{p}_y) = \frac{1}{2\pi i} \int_0^{2\pi} \frac{\gamma(\alpha')}{\eta - z(\alpha')} d\alpha'. \tag{A.3}$$

Here the *vortex sheet strength*  $\gamma$  is related to the dipole strength for  $\tilde{p}$  by  $\gamma = b^2(t)\rho_\alpha$ . Taking the point  $\eta$  to the boundary gives

$$\lim_{\eta \rightarrow z(\alpha)} Q^*|_\eta = \bar{Q}^*|_{\partial\Omega} - \frac{\gamma(\alpha)}{2z_\alpha(\alpha)} + \frac{1}{2\pi i} P \int_0^{2\pi} \frac{\gamma(\alpha')}{z(\alpha) - z(\alpha')} d\alpha' \tag{A.4}$$

and the boundary condition can be written as

$$-b^2\tilde{\tau}\kappa_s = -b^2p_s = \mathbf{u} \cdot \mathbf{s} = \text{Re} \left\{ \frac{z_\alpha}{s_\alpha} Q^*|_{\partial\Omega} \right\}. \tag{A.5}$$

Defining  $\alpha$  as the Lagrangian variable, and substituting  $Q^*$  and  $\bar{Q}^*$  into equations (A.4) and (A.5) gives

$$z_t^* = -\frac{\dot{b}}{2b}z^* - \frac{\gamma(\alpha)}{2z_\alpha(\alpha)} + \frac{1}{2\pi i} P \int_0^{2\pi} \frac{\gamma(\alpha')}{z(\alpha) - z(\alpha')} d\alpha' \tag{A.6}$$

$$\frac{\gamma(\alpha)}{2} - \text{Re} \left\{ \frac{z_\alpha(\alpha)}{2\pi i} P \int_0^{2\pi} \frac{\gamma(\alpha')}{z(\alpha) - z(\alpha')} d\alpha' \right\} = b^2\tilde{\tau}\kappa_\alpha - \frac{\dot{b}}{2b} \text{Re}\{z^*z_\alpha\} \equiv R_\alpha. \tag{A.7}$$

Hence, to advance the position of the interface we first solve the equation (A.7) for  $\gamma$  and then advance the interface position through equation (A.6). However, the integral equation (A.7) has a nontrivial homogeneous solution  $\bar{\gamma}$ , and so the general solution is not unique. We rewrite equation (A.7) in the form

$$\frac{1}{2}\gamma(\alpha) - \int_0^{2\pi} K(\alpha, \alpha')\gamma(\alpha') d\alpha' = R_\alpha. \tag{A.8}$$

While it is not obvious, the kernel  $K(\alpha, \alpha')$  is continuous for any periodic  $z \in C^3([0, 2\pi])$  and is thus square integrable. This means that the Fredholm alternative can be applied. The homogeneous adjoint equation is

$$\frac{1}{2}\beta(\alpha') - \text{Re} \left\{ \frac{1}{2\pi i} P \int_0^{2\pi} \frac{z_\alpha(\alpha)}{z(\alpha) - z(\alpha')} \beta(\alpha) d\alpha \right\} = 0 \tag{A.9}$$

and it can be shown that it has only the solution  $\beta \equiv \text{constant}$ . Solvability of equation (A.7) is guaranteed, as the integral of its right-hand side ( $R_\alpha$ ) against the constant  $\beta$  is zero. And so, the general solution to equation (A.7) can be given as  $b^2(t)\rho_\alpha + A\bar{\gamma}$ . It can be shown that  $\bar{\gamma}$  is of nonzero mean, and so requiring that

$$\int_0^{2\pi} d\alpha \gamma(\alpha) = 0$$

sets  $A$  to zero, and yields the desired solution.

## References

- [1] Almgren R 1996 Singularity formation in Hele–Shaw bubbles *Phys. Fluids A* **8** 344–52
- [2] Almgren R, Bertozzi A and Brenner M 1996 Stable and unstable singularities in the unforced Hele–Shaw cell *Phys. Fluids A* **8** 1356
- [3] Baker G R and Shelley M J 1986 Boundary integral techniques for multi-connected domains *J. Comput. Phys.* **64** 112
- [4] Baker G R and Shelley M J 1990 On the connection between thin vortex layers and vortex sheets *J. Fluid Mech.* **215** 161

- [5] Ben Amar M, Hakim V, Mashaal M and Couder Y 1991 Self-dilating viscous fingers in wedge-shaped Hele–Shaw cells *Phys. Fluids A* **3** 2039
- [6] Ben-Jacob E, Godbey R, Goldenfeld N D, Koplik J, Levine H, Mueller T and Sanders M 1985 Experimental demonstration of the role of anisotropy in interfacial pattern formation *Phys. Rev. Lett.* **55** 1315
- [7] Bertozzi A L, Brenner M P, Dupont T F and Kadanoff L P 1994 Singularities and similarities in interface flows *Trends and Perspectives in Applied Mathematics (Applied Mathematics Series)* ed L Sirovich (New York: Springer)
- [8] Bertozzi A L and Constantin P 1993 Global regularity for vortex patches *Commun. Math. Phys.* **152** 19–28
- [9] Carrier G, Krook M and Pearson C 1966 *Functions of a Complex Variable* (New York: McGraw-Hill)
- [10] Chemin J-Y 1993 Persistence de structures geometriques dans les fluides incompressibles bidimensionnels *Ann. l'Ecole Normale Supérieure* **26** 1–16
- [11] Cherednichenko V G 1976 The solvability ‘in the small’ of the inverse problem for a potential with variable density in the two-dimensional case *Sibirsk. Mat. Zh.* **17** 863–70
- [12] Constantin P, Dupont T, Goldstein R, Kadanoff L, Shelley M J and Zhou S 1993 Droplet breakup in a model of the Hele–Shaw cell *Phys. Rev. E* **47** 4169  
See also Dupont T, Goldstein R, Kadanoff L and Zhou S 1993 *Phys. Rev. E* **47** 4182
- [13] Dai W-S, Kadanoff L P and Zhou S-M 1991 Interface dynamics and the motion of complex singularities *Phys. Rev. A* **43** 6672
- [14] Dai W S and Shelley M J 1993 A numerical study of the effect of surface tension and noise on an expanding Hele–Shaw bubble *Phys. Fluids A* **5** 2131
- [15] Entov V M, Etingof P I and Kleinbock D Ya 1995 On nonlinear interface dynamics in Hele–Shaw flows *Eur. J. Appl. Math.* **6** 399
- [16] Goldstein R, Pesci A and Shelley M 1993 Topological transitions and singularities in viscous flows *Phys. Rev. Lett.* **70** 3043  
See also Goldstein R, Pesci A and Shelley M 1995 Attracting manifold for a viscous topology transition *Phys. Rev. Lett.* **75** 3665
- [17] Hou T Y, Lowengrub J S and Shelley M J 1994 Removing the stiffness from interfacial flows with surface tension *J. Comput. Phys.* **114** 312
- [18] Krasny R 1986 A study of singularity formation in a vortex sheet by the point vortex approximation *J. Fluid Mech.* **167** 65
- [19] Kellogg D *Foundations of Potential Theory* (New York: Dover)
- [20] Langer S A, Goldstein R E and Jackson D P 1992 Dynamics of labyrinthine pattern formation in magnetic fluids *Phys. Rev. A* **46** 4894
- [21] Louis E, Pla O, Sander L M and Guinea F 1994 Variations on the theme of diffusion-limited aggregation *Mod. Phys. Lett. B* **8** 1739
- [22] McCloud K V and Maher J V 1995 Experimental perturbations to Saffman–Taylor flow *Phys. Rep.* **260** 139–85
- [23] Nie Q and Tian F R 1998 Singularities in Hele–Shaw flows *SIAM J. Appl. Math.* to appear
- [24] Richardson S 1972 Hele–Shaw flows with a free boundary produced by the injection of fluid into a narrow channel *J. Fluid Mech.* **56** 609–18
- [25] Richardson S 1981 Some Hele–Shaw flows with time-dependent free boundaries *J. Fluid Mech.* **102** 263–78
- [26] Saad Y and Shultz M 1986 GMRES: a generalized minimal residual algorithm for solving nonsymmetric linear systems *SIAM J. Sci. Stat. Comput.* **7** 856–69
- [27] Sakai M 1978 A moment problem on Jordan domains *Proc. AMS* **70** 35–8
- [28] Shraiman B and Bensimon D 1984 *Phys. Rev. A* **30** 2480
- [29] Sidi A and Israeli M 1988 Quadrature methods for periodic singular and weakly singular Fredholm integral equations *J. Sci. Comput.* **3** 201–31
- [30] Sonin A and Bartolino R 1993 Air viscous fingers in isotropic fluid and liquid crystals obtained in lifting Hele–Shaw cell geometry *Nuovo Cimento Soc. Ital. Fis. D* **15**
- [31] Tian F R 1995 On the breakdown of Hele–Shaw solutions with non-zero surface tension I. *Nonlinear Sci.* **5** 479–84
- [32] Tian F R 1996 A Cauchy integral approach to Hele–Shaw Problems with a free boundary: the zero surface tension case *Arch. Rat. Mech. Anal.* **135** 175–96
- [33] Tryggvason G and Aref H 1983 Numerical experiments on Hele–Shaw flow with a sharp interface *J. Fluid Mech.* **136** 1
- [34] Varchenko A N and Etingof P I 1992 *Why the Boundary of a Round Drop becomes a Curve of Order Four* (Providence, RI: American Mathematical Society)
- [35] Experiments by Woods A 1993 *GFD Summer School* Woods Hole Oceanographic Institute

- [36] Zhao H, Casademunt J, Yeung C and Maher J V 1992 Perturbing Hele–Shaw flow with a small gap gradient  
*Phys. Rev. A* **45** 2455–60
- [37] Zabusky N, Hughes M and Roberts K 1979 Contour dynamics for the Euler equations in two dimensions  
*J. Comput. Phys.* **30** 96